applied sciences

MDPI

Article

Energy-Based Fatigue Assessment of Defect-Afflicted Cast Steel Components by Means of a Linear-Elastic Approach

Michael Horvath *, Matthias Oberreiter and Michael Stoschka

Christian Doppler Laboratory for Manufacturing Process Based Component Design, Chair of Mechanical Engineering, Montanuniversität Leoben, Franz-Josef-Strasse 18, 8700 Leoben, Austria
* Correspondence: michael.horvath@unileoben.ac.at; Tel.: +43-3842-402-1480

Abstract: Cast steel components are affected by manufacturing process-based imperfections, which severely limit their fatigue strength. In this work, the linear-elastic strain energy density concept is applied to assess the fatigue behaviour of bulk defect-afflicted components made of high-strength cast steel alloy G12MnMo7-4+QT. Based on analytical calculations, an energy-based design limit curve is derived which merges experimental results of notched and unnotched small–scale specimens into a statistically proven scatter band. The stress ratio dependency is also investigated. Moreover, a numerical methodology is introduced, which facilitates the energy-based fatigue assessment of complex spatial imperfections on the basis of radiographs. Validation of the established framework utilizing experimental results of defect-afflicted large–scale specimens leads to sound accordance of numerically and experimentally derived fatigue strength values, showing an average deviation of about only eight percent.

Keywords: cast steel; local fatigue assessment; defects; strain energy density

Citation: Horvath, M.; Oberreiter, M.; Stoschka, M. Energy-Based Fatigue Assessment of Defect-Afflicted Cast Steel Components by Means of a Linear-Elastic Approach. *Appl. Sci.* **2023**, *13*, 3768. https://doi.org/10.3390/app13063768

Academic Editor: Alberto Campagnolo

Received: 2 February 2023
Revised: 10 March 2023
Accepted: 13 March 2023
Published: 15 March 2023

1. Introduction

Modern production technologies focus on the economic and sustainable design of components in mass-production. This often yields complex-shaped components and high local load factors of corresponding cross-sections. Due to their high-load-bearing capabilities at moderate costs, cast steel alloys are widely utilized in lightweight design [1–4]. The degree of complexity in geometric shape severely affects process parameters such as the local solidification rate, which provokes the formation of manufacturing process-based imperfections during the solidification of cast steel components [5]. As the size of respective defect structures often reaches dimensions of several millimetres, the local acting stress field is altered significantly, resulting in severely limited fatigue strength of defect-afflicted cast steel components [6–11]. In order to assure the operationally durable design of imperfective components, the commonly utilized engineering guideline FKM (Forschungskuratorium Maschinenbau) proposes safety factors, that depend on the utilized methods of non-destructive testing during the quality control of cast steel components [12]. However, the application of such general safety factors often results in a highly conservative design of mechanical structures, leading to overweight components, which represent a contradiction to modern lightweight design efforts. Hence, the application of local fatigue assessment methods which consider the complex geometric shape of spatial imperfections is beneficial.

Taylor's theory of critical distances (TCD) depicts a widely utilized methodology to assess the fatigue strength of components affected by a stress concentrator, such as a notch [13]. Regarding the therein formulated point method, the concept states that the linear-elastic stress at a certain distance from the notch apex equals the fatigue strength of the plain material $\Delta\sigma_0$, if the component is dimensioned against threshold condition $\Delta K_{th,lc}$ in terms of fatigue crack initiation. The critical distance between the evaluation

point and the notch root is proportional to the material intrinsic length a_0, also known as the El-Haddad length [14], which is given by Equation (1).

$$a_0 = \frac{1}{\pi}\left(\frac{\Delta K_{th,lc}}{\Delta \sigma_0}\right)^2 \quad (1)$$

The TCD is comprehensively applied and validated for static and dynamic analysis of notched components [15–25]. More recently, the methodology was applied to predict the fatigue strength of cast steel components affected by bulk imperfections based on two-dimensional radiographs [26].

The strain energy density (SED) concept constitutes another local fatigue assessment methodology, which facilitates a uniform assessment of arbitrary geometrical configurations subjected to varying loading conditions. The methodology states that fatigue strength of a component is controlled by the strain energy density averaged over the control volume Ω, which represents a finite volume in the vicinity of the assessed stress concentrator, such as a blunt V-notch. Figure 1 depicts a blunt V-notch which is characterized by the notch opening angle 2α, the notch root radius ρ and the notch depth.

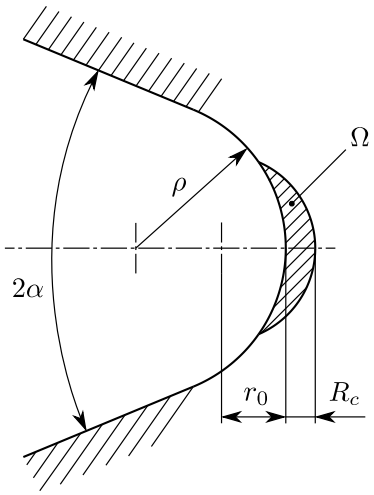

Figure 1. Control volume Ω of a blunt V-notch.

The position of its centre is defined by the parameter r_0, which depends both on 2α and ρ [27]. The size of the control volume determines the aggregated amount of strain energy considered for fatigue assessment and is described by the material dependent control radius R_c. Hence, the evaluation of an appropriate control radius plays a decisive role for energy-based fatigue assessment. Lazzarin et al. [28] presented an analytical solution for the determination of R_c applicable for cracks and V-notches. Equation (2) can be utilized for the evaluation of R_c, invoking the material threshold and endurance limit [28].

$$R_c = \left(\frac{\sqrt{2e_1}\cdot \Delta K^V_{I,th}}{\Delta \sigma_0}\right)^{\frac{1}{1-\lambda_1}} \quad (2)$$

The geometry parameter e_1 depends on the notch opening angle 2α [28], $\Delta K^V_{I,th}$ represents the long-crack growth threshold stress intensity factor range for V-notched components subjected to mode I loading [29] and λ_1 depicts Williams' eigenvalue for mode I loading conditions [30]. Yosibash et al. [31] derived a solution for the determination of R_c by evaluating the SED for a specimen featuring a straight edge (representing a notch opening angle of $2\alpha = 180°$) and a specimen featuring a crack (depicting a notch opening angle of $2\alpha = 0°$). As the critical value of the SED is independent of 2α, equating the SED results of corresponding specimens yields Equation (3) for the evaluation of R_c.

$$R_c = \frac{(1+\nu)(5-8\nu)}{4\pi}\left(\frac{\Delta K_{th,lc}}{\Delta\sigma_0}\right)^2 \tag{3}$$

Comparing Equation (3) to Equation (1) and considering a Poisson's ratio for metallic materials of $\nu = 0.3$, one obtains $R_c = 0.845 \cdot a_0$.

Dealing with blunt V-shaped notches, the linear-elastic strain energy density $\overline{W}^{(e)}$ for mode I loading conditions averaged over the control volume Ω can be evaluated by the analytical framework developed by Lazzarin and Berto [27], given by Equation (4).

$$\overline{W}^{(e)} = F(2\alpha) \cdot H\left(2\alpha, \frac{R_c}{\rho}\right) \cdot \frac{\sigma_{tip}^2}{E} \tag{4}$$

Herein the parameter σ_{tip} represents the maximum stress at the notch root, which is evaluated utilizing linear-elastic finite element analysis. It should be noted, that $\sigma_{tip} = \Delta\sigma_{tip}$ under tumescent loading at a stress ratio of $R = 0$. The Young's modulus E is the result of tensile testing and the parameters $F(2\alpha)$ and $H(2\alpha, R_c/\rho)$ depict functions that depend on the notch geometry and control radius. Values for F and H are reported in the literature [27,32,33] for a variety of notch opening angles and control to notch root radius fractions. Concerning plain specimens subjected to uniaxial tensile loading, the evaluation of the linear-elastic strain energy density range takes on a simplified form given by Equation (5).

$$\Delta\overline{W}^{(e)} = \int_0^{\Delta\varepsilon} \Delta\sigma d\varepsilon = \frac{\Delta\sigma^2}{2E} \tag{5}$$

As the SED represents the area underneath the stress–strain curve [34], the linear-elastic definitions given by Equations (4) and (5) are strictly only valid for tumescent loading at a stress ratio of $R = 0$. In order to enhance the analytical framework to other stress ratios, Lazzarin et al. [35] introduced the mean stress correction coefficient c_w, which relates the linear-elastic SED at a given stress ratio to the one obtained at $R = 0$. During analysis, Equations (4) and (5) are multiplied by c_w, defined by Equation (6). The definition of the linear-elastic SED under consideration of R according to c_w is depicted in Figure 2. As the applied stress range $\Delta\sigma$ is identical for the exemplified cases, the effect of R can be perceived clearly.

$$c_w = \begin{cases} \frac{1+R^2}{(1-R)^2} & R < 0 \\ \frac{1-R^2}{(1-R)^2} & 0 \leq R \leq 1 \end{cases} \tag{6}$$

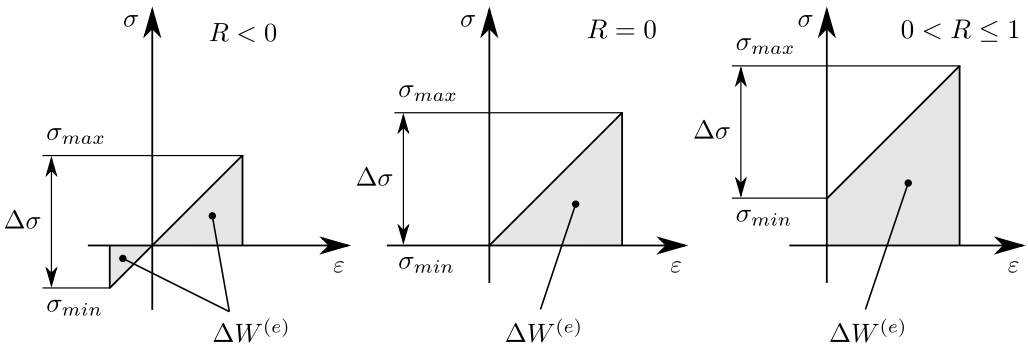

Figure 2. Linear-elastic strain energy density under cyclic loading at different stress ratios.

Based on the analytical framework reported in the literature, the linear-elastic SED concept depicts an engineering-feasible tool for the fatigue assessment of notched or notch-like components, such as welded structures. The methodology has been successfully

applied to a variety of materials and boundary conditions, including elevated-temperature environments and multiaxial loading investigations [36–44].

However, considering arbitrary spatial imperfections inherent in cast steel components, the evaluation of the perturbing influence of defect structures on the acting stress field relies on finite element analyses. These numerical evaluations require information about the geometric shape of the corresponding imperfections. As computer tomography investigation depicts a costly and time-consuming non-destructive testing method, X-ray examinations come to mind next, providing two-dimensional projections of the spatial defect structures. Since the reduction in dimensionality represents a certain loss of information about the geometric defect shape, a methodology to apply the linear-elastic SED concept on plane radiographs has to be established and validated for cast steel specimens containing shrinkage imperfections.

Hence, the present work contributes to the following scientific topics:

- Evaluation of a design limit curve for the investigated high-strength cast steel alloy G12MnMo7-4+QT based on the linear-elastic strain energy density approach.
- Development and validation of an energy-based methodology to assess the fatigue strength of imperfective cast steel specimens based on X-ray radiographs.
- Comparison of the numerical results obtained by the established framework to fatigue assessment results based on the theory of critical distances.

2. Materials and Methods

The alloy G12MnMo7-4+QT in quenched and tempered heat treatment condition was chosen to investigate the influence of macroscopic imperfections on the fatigue strength of cast steel. This cast steel alloy is typically used in railway applications, where high-load cycle numbers are aggregated during operation and defect-induced failure is accompanied by severe consequences. Hence, the appropriate fatigue design of defect-afflicted components is of utmost importance to ensure safe operation. Preceding quasi-static tensile tests revealed a yield strength of $\sigma_{YS} = 549\,\mathrm{MPa}$ and an ultimate tensile strength of approximately $\sigma_{UTS} = 667\,\mathrm{MPa}$, at an elongation at fracture of 22%. The chemical composition of the investigated alloy according to the standard SEW 520 [45] is given in Table 1.

Table 1. Chemical composition in weight percent of the investigated cast steel alloy.

G12MnMo7-4+QT	C	Si	Mn	P	S	Cr	Mo	Nb	V	N
max.	0.15	0.60	1.80	0.02	0.015	0.20	0.40	0.05	0.10	0.02
min.	0.08		1.50				0.30			

To derive the material parameters necessary for the set up of the linear-elastic SED-framework, high-cycle fatigue as well as crack propagation experiments under mode I loading conditions were conducted.

2.1. Characterization of the High-Cycle Fatigue Strength of Plain and Notched Specimens

In order to evaluate the fatigue strength $\Delta\sigma_0$ of the investigated material, high-cycle fatigue experiments were conducted on a RUMUL® Testronic 150 kN (Russenberger Prüfmaschinen AG, Neuhausen am Rheinfall, Switzerland) resonance test rig at room temperature. The specimens were manufactured from bulk material and featured three different geometries, as depicted in Figure 3.

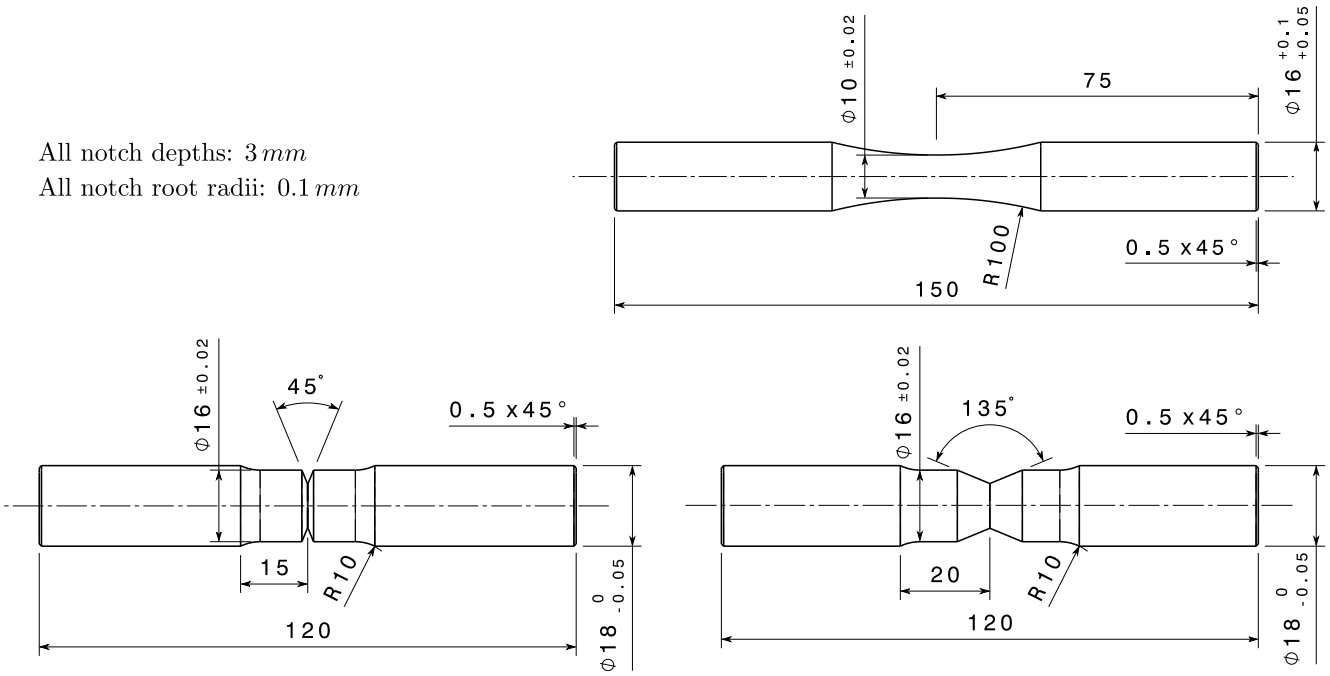

Figure 3. Small–scale specimen geometries utilized for fatigue strength evaluation.

Regarding the characterization of the base material, plain specimens with a diameter of 10 mm were utilized. In order to study the effect of notches on the fatigue behaviour, notched specimens featuring a notch opening angle of $2\alpha = 45°$ and $2\alpha = 135°$ were tested. The notch depth and notch root radius were kept constant for each notch geometry, possessing values of 3 and 0.1 mm, respectively. Subsequent to the manufacturing of the notched specimens, tactile measurements utilizing a Mahr® MarSurf LD 130 (Mahr GmbH, Göttingen, Germany) contour measuring machine were conducted in the notch apex region. High-cycle fatigue tests were carried out under constant amplitude, uniaxial tension–compression loading, where specimens were defined as a run-out if the respective experiment reached ten million load cycles. It should be noted, that load levels observed in the experiments refer to the gross-section of the corresponding specimens, namely, the diameter of 10 mm regarding plain specimens and 16 mm in terms of the notched specimen geometries. Each specimen geometry was investigated at stress ratios of $R = -1, 0$ and 0.5, summing to a total of 176 tested specimens, as depicted in Table 2.

Table 2. Number of tested specimens of each specimen geometry.

R [−]	Plain	$2\alpha = 45°$	$2\alpha = 135°$
−1	25	17	18
0	23	17	22
0.5	18	16	20

2.2. High-Cycle Fatigue Investigations of Bulk Defect-Afflicted Specimens

In order to study the effect of arbitrarily shaped spatial imperfections on the fatigue behaviour of cast steel components, preceding research [46] featured a specimen geometry, provoking the formation of macroscopic shrinkage porosities during the casting process. After the successive casting of corresponding specimens, X-ray examinations of each specimen were carried out, to gain information about the geometric shape of any inherent imperfections. Therefore, two perpendicular planes parallel to the specimen axis were considered, providing an orthogonal glimpse of the three-dimensional shape of the respective defect structure. The obtained two-dimensional projections are referred to as X- and Y-view, as schematically depicted in Figure 4, for a representative defect-afflicted speci-

men under uniaxial loading. Concerning reference radiographs included in the standard ASTM E446 [47], the defects investigated in the present study were classified as category C shrinkage imperfections.

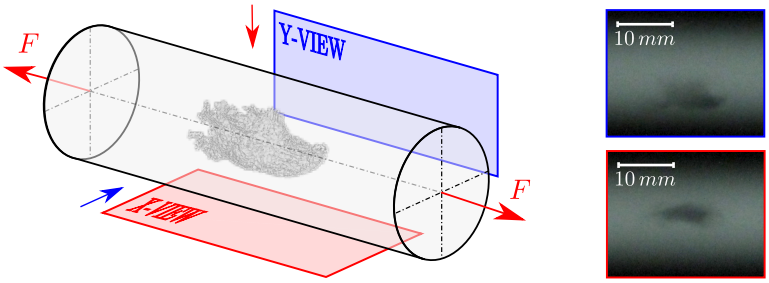

Figure 4. Schematic illustration of the X-ray examination of a representative imperfection.

High-cycle fatigue experiments of defect-afflicted specimens were conducted at room temperature, utilizing a SincoTec® MOT600kN (SincoTec Test Systems GmbH, Clausthal-Zellerfeld, Germany) resonance test rig. Testing was carried out under constant amplitude, uniaxial tension–compression loading at stress ratios of $R = -1$ and 0, resulting in a total count of 33 investigated specimens. The experimental strategy allowed testing individual specimens at a target load level, which ought to result in a run-out of the respective specimen as the number of cycles reached ten million load cycles. Subsequently, the specimen was re-inserted at a higher load level in order to provoke burst failure. Hence, the applied test strategy needed to estimate the load levels for each individual defect, which shall result in a run-out and burst failure of the corresponding imperfection. This pre-fatigue life calculation was performed by invocation of the TCD-method using the two perpendicular X-ray view measurements.

As the imperfections possess an arbitrary spatial shape, the definition of a net cross-section is a complex task. Hence, the investigated load levels refer to the gross-section of the specimens, a diameter of 30 mm, in analogy to the fatigue tests of the parent material reported in Section 2.1. Subsequent to testing, fracture surface analysis utilizing a KEYENCE® VHX-5000 (KEYENCE CORPORATION, Osaka, Japan) digital microscope was conducted, revealing that inherent spatial shrinkage imperfections were the site of fatigue crack initiation in all the investigated specimens. Figure 5 depicts representative fracture surfaces of six specimens tested at stress ratios of $R = -1$ and 0, respectively.

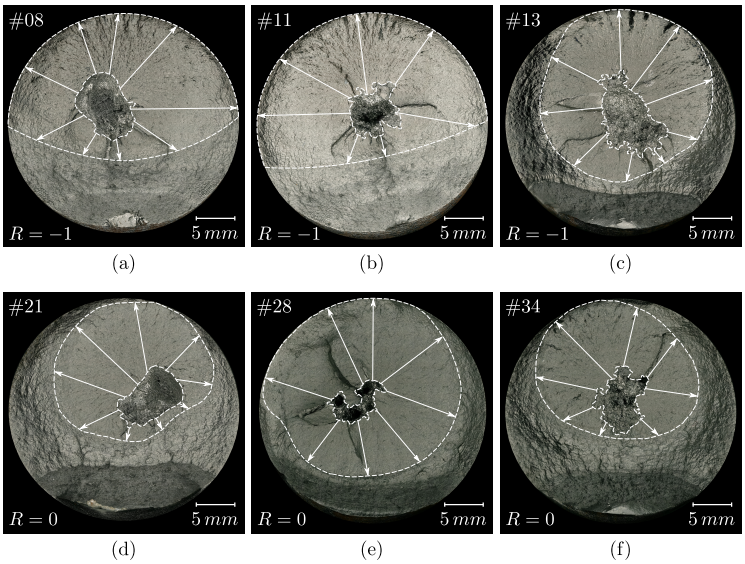

Figure 5. Fracture surfaces of selected defect-afflicted large–scale specimens: (**a**–**c**) Specimens #08, #11 and #13 tested at $R = -1$; and (**d**–**f**) Specimens #21, #28 and #34 tested at $R = 0$.

2.3. Fracture Mechanical Investigations

Considering Equation (3), the control radius R_c necessary for application of the linear-elastic SED concept depends on the long-crack growth threshold stress intensity factor range $\Delta K_{th,lc}$. Hence, fracture mechanical investigations in terms of crack propagation experiments were conducted to evaluate $\Delta K_{th,lc}$ for the investigated stress ratios of $R = -1, 0$ and 0.5. Single-edge-notched bending samples (SENB) were utilized, as depicted in Figure 6.

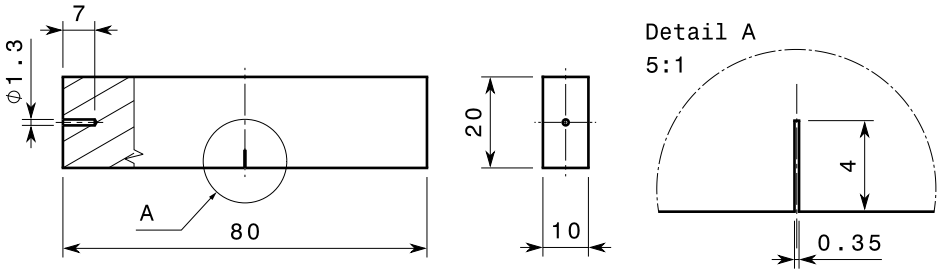

Figure 6. SENB geometry utilized for crack propagation experiments.

After milling of the specimens from bulk material, the initial notch featuring a width of 0.35 mm and a notch depth of 4 mm was manufactured by wire-cut electrical discharge machining, followed by polishing of the sides of the sample geometry. The polishing procedure assisted the measurement of the initial notch geometry by microscopy. In order to achieve a defined pre-crack necessary for subsequent crack propagation experiments, the specimens were razor-blade polished utilizing diamond polishing suspension. The evaluation of $\Delta K_{th,lc}$ was conducted according to the rising load amplitude crack growth test procedure recommended by Tabernig and Pippan [48]. This procedure applies compressive pre-cracking [49,50] of respective specimens, which was carried out on a SincoTec® Power Swing MOT100kN (SincoTec Test Systems GmbH, Clausthal-Zellerfeld, Germany) resonance test rig at a stress ratio of $R = 20$. Subsequently, crack propagation experiments were conducted under constant amplitude loading at room temperature, using a RUMUL® Cracktronic (Russenberger Prüfmaschinen AG, Neuhausen am Rheinfall, Switzerland) resonance test rig. Utilizing a constant stepping of the applied load, the stress intensity factor range ΔK was increased until long-crack propagation occurred. Crack propagation was measured by the direct current potential drop method, incorporating compensation for crack length fluctuations due to ambient temperature changes [51]. Figure 7 depicts crack propagation curves of three representative experiments for the investigated stress ratios.

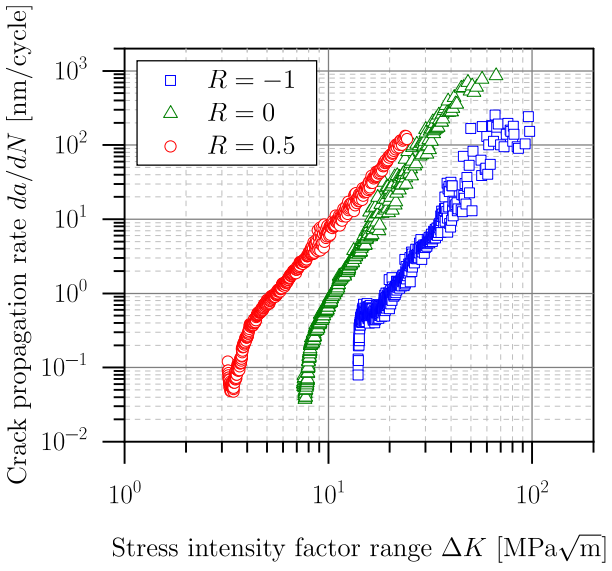

Figure 7. Crack propagation curves for investigated stress ratios.

Regarding Figure 7, the influence of R on the propagation behaviour of fatigue cracks can be perceived clearly. As the value of R increases, contact of the crack flanks during cyclic loading is restricted [52]. Hence, the build-up of crack closure mechanisms, such as plasticity-induced or roughness-induced crack closure, is less pronounced as the crack transitions from short- to long-crack growth, resulting in lower values of $\Delta K_{th,lc}$ [53–55].

The experimental results were evaluated for the investigated stress ratios, where $\Delta K_{th,lc}$ was estimated by a least-mean-squares regression of the NASGRO Equation [54]. The determined values of $\Delta K_{th,lc}$, as well as the number of specimens tested, are listed in Table 3.

Table 3. Results of the evaluation of $\Delta K_{th,lc}$ for the investigated stress ratios.

R [−]	Number of Specimens [−]	$\Delta K_{th,lc}$ [MPa$\sqrt{\text{m}}$]		
		Mean	Minimum	Maximum
−1	4	13.72	13.35	14.03
0	3	7.65	7.54	7.74
0.5	2	3.40	3.36	3.44

As the effect of crack closure mechanisms is less pronounced at higher values of R, the variation of derived threshold values is also reduced, which is given in Table 3 by comparing the min–max range of obtained stress intensity factors. Although the experimental data shows only small scatter indices, the arithmetic mean value of $\Delta K_{th,lc}$ for each investigated stress ratio was utilized for calculations reported in the following sections.

3. Results and Discussion

As the material-dependent input parameters characterizing the fatigue behaviour of the investigated cast steel alloy G12MnMo7-4+QT are now experimentally derived, the linear-elastic SED-framework can be put into operation. The procedure includes the evaluation of a design limit curve based on experimental results of plain and notched specimens as well as the application of the methodology to assess the fatigue strength of defect-afflicted cast steel components.

3.1. Evaluation of the Linear-Elastic Design Limit Curve

In order to describe the control volume governing the aggregated amount of strain energy during fatigue assessment, the control radius R_c was evaluated according to Equations (2) and (3). Additionally to the dependency of the material parameters $\Delta K_{th,lc}$ and $\Delta\sigma_0$ on R, Equation (2) also includes parameters that rely on the geometry of the utilized notched specimens. Hence, the long-crack growth threshold stress intensity factor range for V-notched specimens $\Delta K^V_{I,th}$ as well as the geometry parameter e_1 were evaluated for the notch geometries utilized in the experimental small–scale fatigue tests. The resulting values of R_c are given in Table 4, alongside the calculated values of a_0 according to Equation (1).

Table 4. Results of the evaluation of R_c and a_0.

R [−]	2α [°]	a_0 [mm]	R_c [mm]	
		Equation (1)	Equation (2)	Equation (3)
−1	45 135	0.146	0.138 0.133	0.124
0	45 135	0.097	0.091 0.088	0.082
0.5	45 135	0.039	0.037 0.035	0.033

Regarding the results depicted in Table 4, the calculations according to Equations (2) and (3) result in similar values of the control radius for the investigated stress ratios. Both evaluation methods show decreasing values of R_c as R increases. Recalling Equation (3), R_c is directly connected to the material intrinsic length a_0. Hence, the dependency of R_c upon R reflects the trend of a_0 as reported in the literature [56]. However, calculations of the SED incorporating a control radius that depends on the acting stress ratio resulted in significantly enlarged scattering of the analysed experimental fatigue data. A decrease in R_c resulted in a smaller value of the considered control volume. Due to the stress gradient emanating from the apex of notch-like geometries, a smaller control volume implies an increasing focus on the highly-stressed region in the vicinity of the notch root. Hence, the averaged value of the calculated SED shifts towards higher values, as the size of the control volume decreases. Following this considerations, a larger control volume leads to an underestimation of the calculated averaged SED values. Apart from the variation observed in the calculated SED values, the implementation of a dependency of R_c upon R also significantly increases the experimental effort necessary to establish the respective relationship. Hence, an averaged value of R_c = 0.083 mm was utilized in the present analysis independent of the stress ratio. Considering Table 4, it should be noted that this average value shows only a small deviation to the evaluated values of R_c at a stress ratio of $R = 0$. As $\Delta\sigma_0$ and $\Delta K_{th,lc}$ are often reported in the literature for $R = 0$, an appropriate value of the control radius can be conveniently calculated utilizing Equation (3). However, from a scientific point of view, the study of the relationship between R_c and R depicts an interesting topic for future research work.

As an appropriate value of R_c was defined, the results of the experimental investigations reported in Section 2.1 were evaluated in terms of the linear-elastic strain energy density range $\Delta\overline{W}^{(e)}$. Notched specimens were evaluated in accordance to the analytical framework presented by Lazzarin and Berto [27]. The evaluation of the fatigue test results of the utilized plain specimens was carried out according to Equation (5). The effect of the stress ratio was accounted for by the implementation of the factor c_w, given by Equation (6). Statistical evaluation of the fatigue data was conducted following the standard ASTM E739 [57] in the finite-life region, where the fatigue limit in the high-cycle fatigue regime was determined according to the $arcsin\sqrt{P}$ approach [58]. Figure 8 depicts the assessed fatigue data in terms of the linear-elastic SED.

Figure 8 summarizes the experimentally derived fatigue data into a uniform scatter band, combining the results of three different specimen geometries tested at stress ratios of $R = -1, 0$ and 0.5. The statistically evaluated fatigue limit curve for a probability of survival of $P_S = 50\%$ was plotted, alongside the scatter band representing probabilities of survival of $P_S = 10$ and 90%. Furthermore, the probability of survival of $P_S = 97.5\%$ was evaluated, serving as a design limit curve in accordance to the commonly utilized guideline FKM [12]. Concerning the scatter band index of the depicted data points, the linear-elastic fatigue assessment gave a value of $1 : T_{\Delta\overline{W}^{(e)}} = 4.32$. It should be noted, that the energy-based fatigue assessment implies an increased scatter index of fatigue data compared to stress-based concepts, due to the quadratic relationship between the stress and strain energy density. By calculating the square root of the energy-based scatter index, the scatter index in terms of stresses was computed as a value of $1 : T_\sigma = 2.08$. This comparably high value was mainly caused by the fatigue data evaluated at a stress ratio of $R = 0.5$. Regarding Figure 8, the experimental results at stress ratios of $R = -1$ and 0 revealed an overall match. Only the evaluated SED values of notched specimens tested at $R = 0.5$ diverged significantly from the remaining data points. As the notched specimens exhibited stress concentration at the notch apex, the high values of maximum stresses during cyclic loading at $R = 0.5$ resulted in plastic deformation in the vicinity of the notch root. This plastic deformation caused mean stress relaxation [59,60], leading to cyclic testing under an effective stress ratio of $R < 0.5$, following the initial loading. Hence, as the effect of the stress ratio was implemented in the fatigue assessment by consideration of the factor c_w given by Equation (6), the linear-elastic SED was overestimated. This overestimation

was traced back to the value of c_w, which takes a value of 3 at $R = 0.5$, implying that the linear-elastic SED is three times larger than the one at $R = 0$. In order to improve the prediction accuracy even at high stress ratios, the implementation of the elastic-plastic material behaviour should be considered in further work.

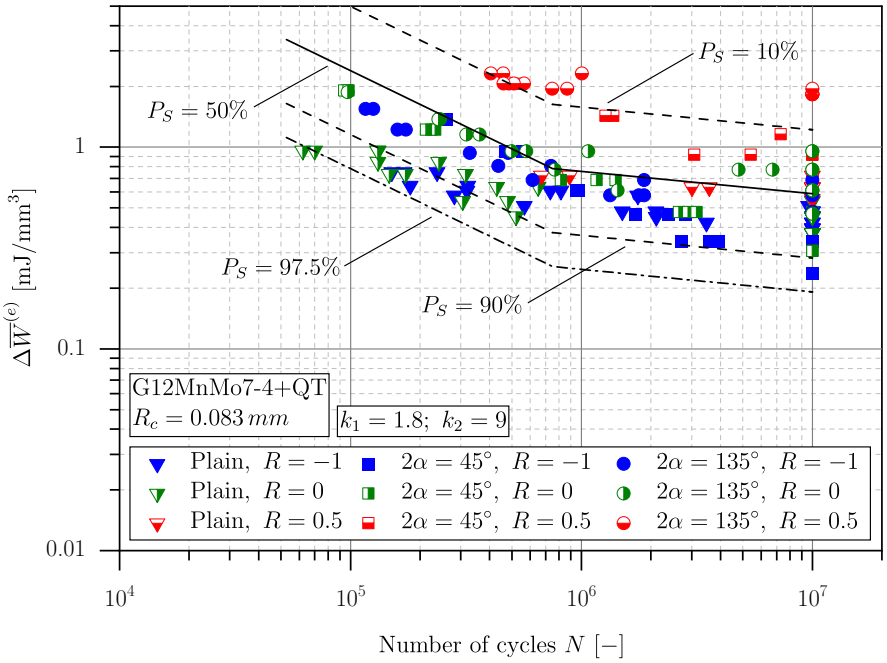

Figure 8. Linear-elastic strain energy density-based design limit curve.

3.2. Calculation of the Linear-Elastic Strain Energy Density of Bulk Defects

Following the definition of the linear-elastic design limit curve, the methodology was extended to assess the fatigue strength of defect-afflicted specimens considered in Section 2.2. Following the considerations of a preceding study [26], a numerical assessment strategy was formulated. As the evaluation of the fatigue behaviour bases on the geometrical appearance of the inherent imperfections, the two recorded radiographs, denoted as X- and Y-view were digitalized for each imperfect large–scale specimen. Due to the discrete nature of the digital images, a smoothing algorithm [61] was applied to derive continuous defect contours. Subsequently, geometrical shape parameters of the digitalized defect structures were calculated in order to characterize the depicted imperfections on the assessed radiographs. Table 5 summarizes the minimum and maximum values of the respective shape parameters derived from the 66 assessed radiographs of the present numerical study.

Table 5. Shape parameters of assessed defect projections.

Parameter	Minimum	Maximum
Area [mm^2]	53.97	227.58
Feret Max. [mm]	11.15	61.13
Feret Min. [mm]	4.80	11.64
Aspect ratio [−]	1.72	7.46
Circularity [−]	0.08	0.75
Convexity [−]	0.30	0.99
Elongation [−]	2.30	24.06

The numerical calculations were conducted by linear-elastic finite element analyses utilizing the software package Abaqus® 2021. As the radiographs depict two-dimensional projections of the corresponding imperfection, planar simulation models were utilized,

in which the respective defect structures were implemented, respectively. Concerning the angular orientation of the defect contour, the rotation angle reflects the one investigated in the experiments described in Section 2.2. Plane stress elements with quadratic shape functions of type CPS6/CPS8 were used. It should be noted, that the size of the finite element models as well as the element sizes were proportional to the absolute dimensions of the corresponding defect in order to provide a simulation methodology that was applicable to arbitrary defect structures. The numerical models were loaded under uniaxial tension, evoking a maximum stress of 1 MPa in the gross-section of the model. Figure 9 depicts the simulation results of selected defect structures. The evaluated stress constitutes the stress concentration factor induced by the respective imperfections.

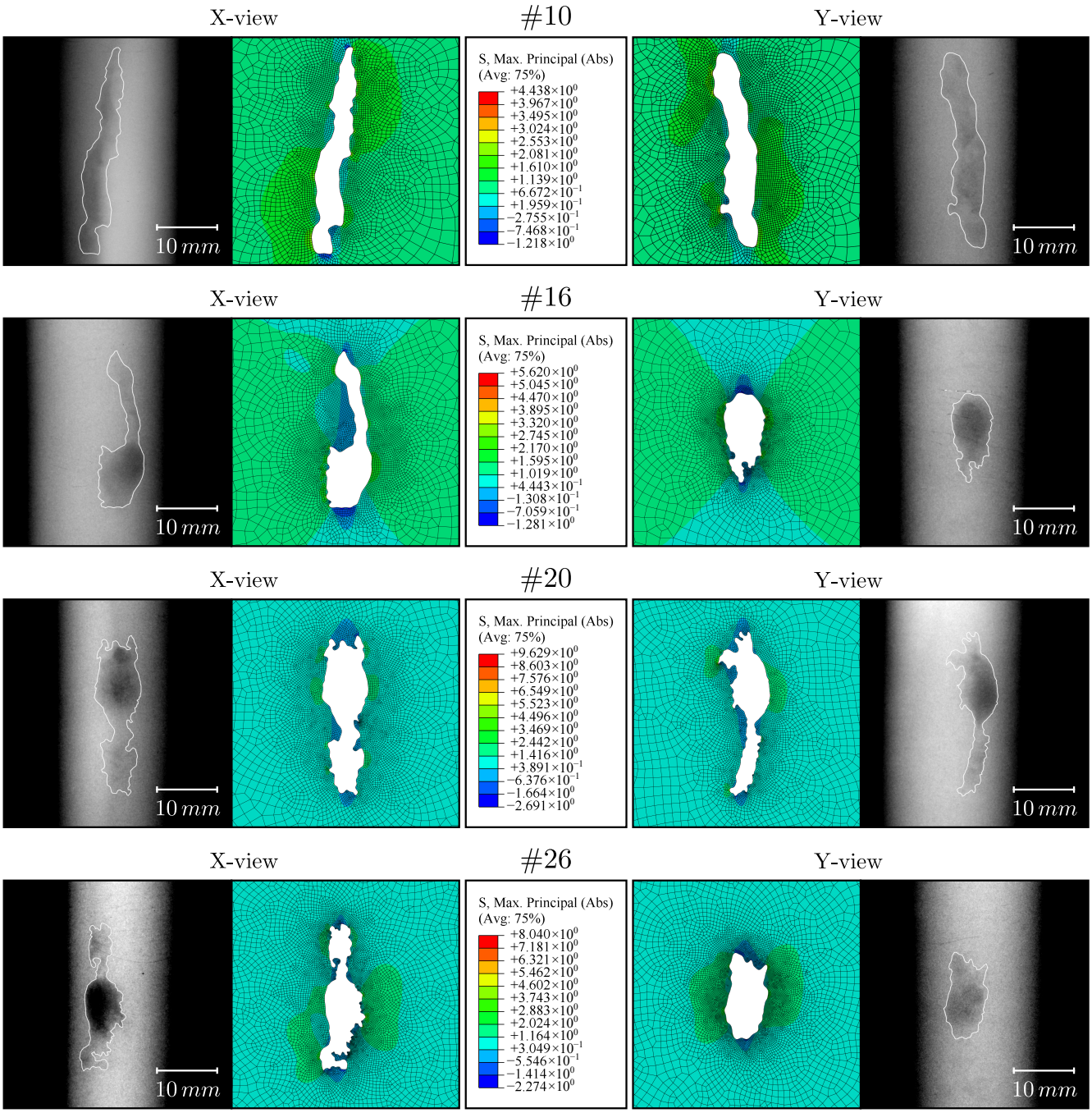

Figure 9. Numerical results based on the radiographs of specimens #10, #16, #20 and #26.

As the numerical simulations represent static analyses, the SED evoked by the maximum stress of 1 MPa can be interpreted as the cyclic SED induced due to an acting stress range of $\Delta\sigma_g = 1$ MPa at a stress ratio of $R = 0$. Due to the linear-elastic material behaviour considered in the numerical analyses, the evaluated strain energy density values can be conveniently scaled to load levels investigated in the corresponding experiments.

As the spatial imperfections possess an irregular shape, the planar projections also feature an arbitrary contour, which leads to a wide variability in the observed SED values. In order to derive a characteristic assessment parameter that reflects the fatigue behaviour of the defect-afflicted specimens, a statistical evaluation of the SED distribution along the defect contour was conducted. This procedure includes the definition of a control volume, which moves along the nodes of the respective projection contour. In order to provide a numerically efficient assessment methodology, finite element sub-modelling technique was applied. Figure 10 summarizes the numerical simulation strategy.

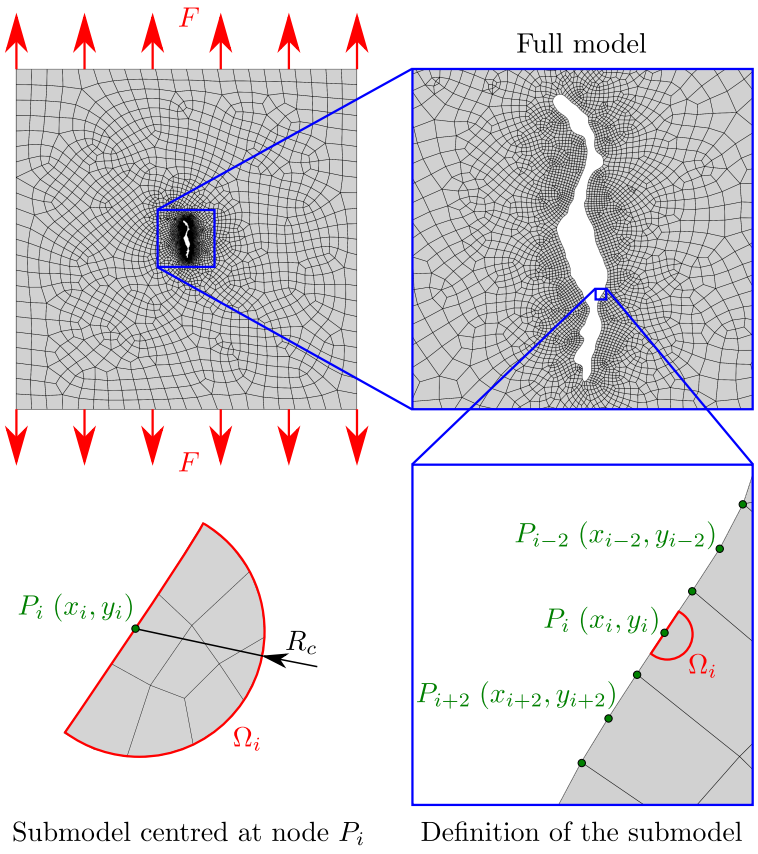

Figure 10. Simulation strategy to assess defect-afflicted cast steel specimens.

At first, the stress field induced by the defect contour was calculated featuring a relatively coarse mesh in the neighbourhood of the imperfection. Subsequently, a sub-model was defined, which represents the control volume Ω_i utilized for calculating the linear-elastic SED. In analogy to the definition of the control volume at sharp notches [28], the utilized control volume was centred in a node P_i of the respective defect contour, where the size of the control volume was defined by R_c, evaluated in Section 3.1. A minimum of three elements were utilized within the control volume, as suggested in [24,62]. Compared to stress-based concepts, obtained SED results were not significantly affected by the size of the finite elements. Hence, rather coarse element sizes could be utilized without sacrificing accuracy. After defining the control volume, the sub-model was analysed and the averaged SED $\Delta\overline{W}_i^{(e)}$ was calculated from the numerical results of the elements defining Ω_i. The procedure was then repeated for the next node P_{i+1} along the defect contour, until the whole perimeter of the planar projection was assessed. The representative fatigue

parameter $\Delta\overline{W}^{(e)}_{97.5\%}$ was defined as the SED value, exceeding 97.5% of all values along the defect contour. Figure 11 presents the determination of $\Delta\overline{W}^{(e)}_{97.5\%}$ through the example of the defect contour found on the Y-view of specimen #26. The left-hand side depicts the contour plot of $\Delta\overline{W}^{(e)}_{i}$ along the perimeter of the imperfection, while the diagram on the right-hand side shows the evaluation of $\Delta\overline{W}^{(e)}_{97.5\%}$ based on the discrete numerical results.

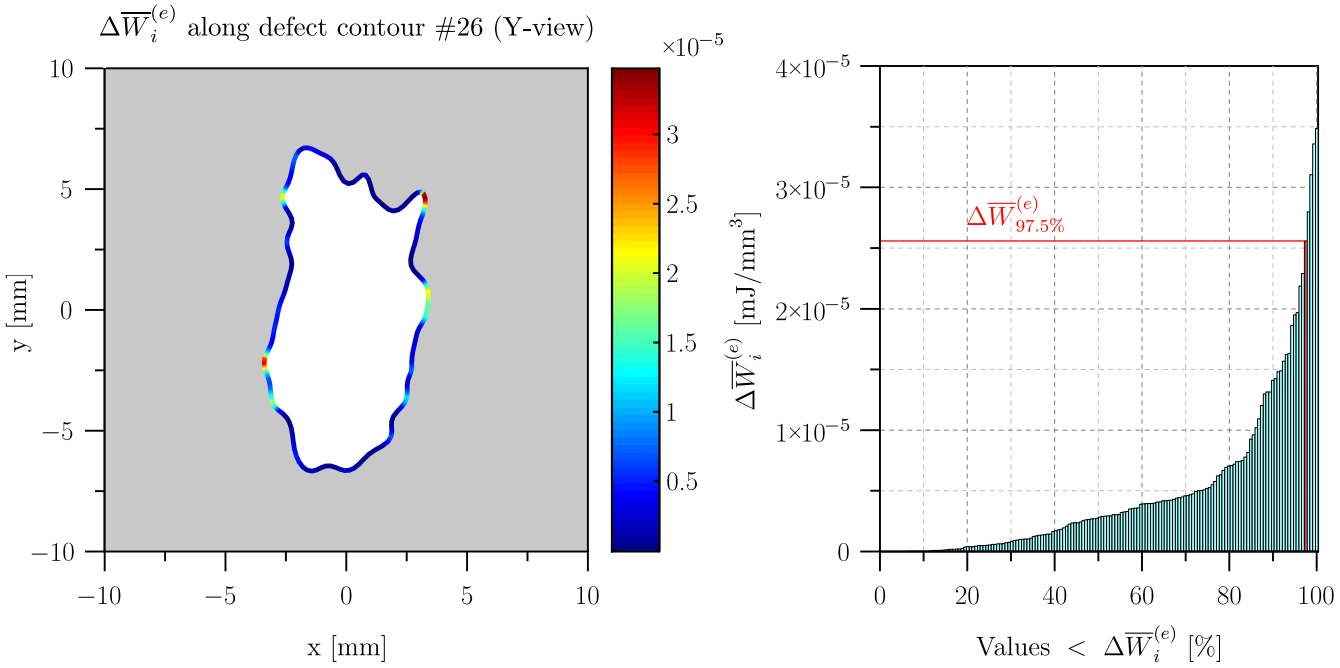

Figure 11. Evaluation of the fatigue parameter $\Delta\overline{W}^{(e)}_{97.5\%}$ exemplified on the Y-view of specimen #26.

It should be emphasized, that $\Delta\overline{W}^{(e)}_{97.5\%}$ was evaluated utilizing a gross stress of $\Delta\sigma_g = 1$ MPa. Due to the linear-elastic finite element analyses involved in the determination of $\Delta\overline{W}^{(e)}_{97.5\%}$, the fatigue strength $\Delta\sigma_{LLF,Defect}$ of the respective defect-afflicted specimen can be calculated following Equation (7), where $\Delta\sigma_0$ represents the fatigue strength of the plain material at the stress ratio R to be assessed.

$$\Delta\sigma_{LLF,Defect} = \sqrt{\frac{\left(\Delta\sigma_0 \cdot \Delta\sigma_g\right)^2}{2E \cdot \Delta\overline{W}^{(e)}_{97.5\%}}} \tag{7}$$

3.3. Validation of the Calculated Fatigue Strength Results

Validation of the proposed fatigue assessment methodology was conducted utilizing the results of the high-cycle fatigue experiments presented in Section 2.2. The fatigue strength of corresponding specimens was evaluated according to the procedure described in Section 3.2 and compared to the load levels investigated in the experiments. Figure 12 summarizes the validation results for stress ratios of $R = -1$ and 0, respectively.

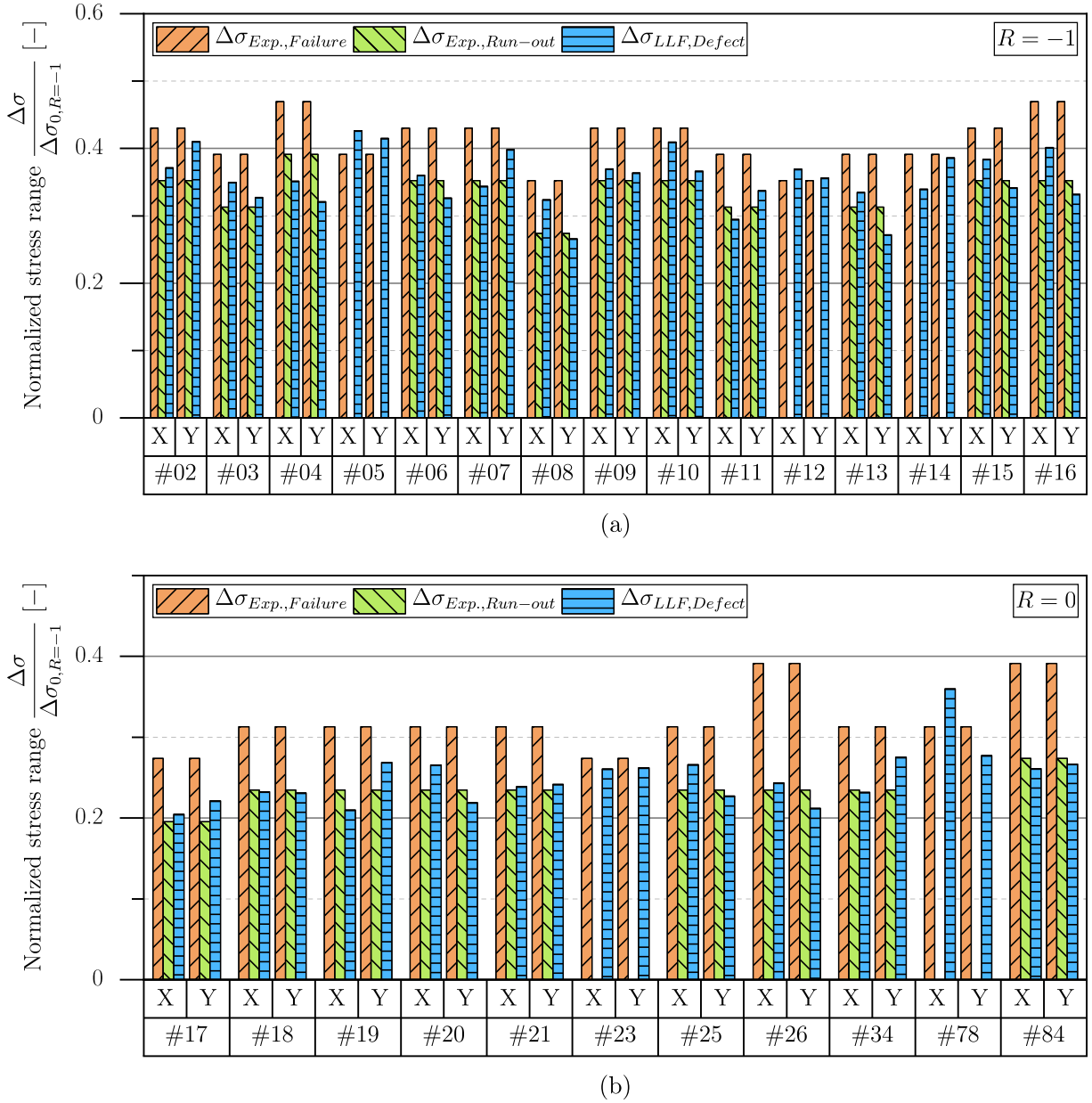

Figure 12. Validation results of the SED analysis of defect-afflicted cast steel specimens: (**a**) Specimens tested at $R = -1$; and (**b**) specimens tested at $R = 0$.

Herein, the abscissa depicts the individual specimens in terms of the utilized radiographs denoted as X- and Y-view, which were assessed by the presented methodology. The parameter $\Delta\sigma_{Exp.,Failure}$ represents the stress range, which led to burst failure in the corresponding experiment. $\Delta\sigma_{Exp.,Run\text{-}out}$ depicts the stress range, where a run-out of the respective specimen at ten million load cycles was achieved. $\Delta\sigma_{LLF,Defect}$ represents the assessed fatigue strength of the defect-afflicted specimen, evaluated by the established SED-framework. All depicted stress ranges were normalized with respect to the fatigue strength $\Delta\sigma_{0,R=-1}$ of the parent material at a stress ratio of $R = -1$. Considering the depicted results, the presented energy-based fatigue assessment methodology leads to a sound agreement of estimated fatigue strength values and experimental results, as $\Delta\sigma_{LLF,Defect}$ is either smaller than $\Delta\sigma_{Exp.,Run\text{-}out}$ or takes a value between $\Delta\sigma_{Exp.,Run\text{-}out}$ and $\Delta\sigma_{Exp.,Failure}$. Regarding the second case, it should be noted, that the depicted values of $\Delta\sigma_{Exp.,Run\text{-}out}$ are not necessarily the highest possible load levels to achieve a run-out of the corresponding specimens, as the specimens were re-inserted to provoke burst failure after a run-out was

observed. Hence, values of $\Delta\sigma_{LLF,Defect}$ that lie in between $\Delta\sigma_{Exp.,Run\text{-}out}$ and $\Delta\sigma_{Exp.,Failure}$ depict plausible fatigue strength estimations of the respective specimens. Taking a closer look at Figure 12, one obtains a few specimens, where no run-out was achieved. These supposedly non-conservative assessment results are also reported in Table 6.

Table 6. Number of load cycles to burst failure.

R $[-]$	Specimen	Cycles to Failure $[-]$
-1	#02	3,335,750
	#03	3,352,772
	#04	13,076
	#05	9,708,502
	#06	2,336,391
	#07	1,135,902
	#08	7,876,634
	#09	540,942
	#10	2,533,432
	#11	5,063,835
	#12	9,526,277
	#13	912,933
	#14	6,880,565
	#15	2,591,440
	#16	3,645,336
0	#17	6,671,185
	#18	954,420
	#19	581,208
	#20	2,789,243
	#21	2,008,825
	#23	8,364,431
	#25	3,232,072
	#26	16,900
	#34	2,616,984
	#78	2,964,118
	#84	195,189

Regarding specimens #05, #12 and #23, the achieved numbers of cycles where burst failure occurred were quite close to ten million cycles, which serves as a criterion of a run-out. As the deviations between $\Delta\sigma_{LLF,Defect}$ and $\Delta\sigma_{Exp.,Run\text{-}out}$ were quite small, the presented values of $\Delta\sigma_{LLF,Defect}$ depict plausible estimations of the fatigue strength. Considering specimens #14 and #78, the numbers of cycles to failure show values of approximately 6.88 and $2.96 \cdot 10^6$ and therefore a higher divergence to the run-out criterion. However, the depicted values of $\Delta\sigma_{LLF,Defect}$ regarding the X-view of specimen #14 as well as the Y-view of specimen #78 propose a fatigue strength, that is quite below the observed stress range at burst failure. Hence, the presented values of $\Delta\sigma_{LLF,Defect}$ also depict reasonable fatigue strength estimations, as experiments utilizing a stress range of $\Delta\sigma_{LLF,Defect}$ could have achieved run-outs of the respective specimens.

As exemplified by specimens #14 and #78, the fatigue strength simulation results based on the X- and Y-view of the corresponding specimens differ from each other in some cases. Hence, the derived values of $\Delta\sigma_{LLF,Defect}$ can be classified in two groups, namely, lower and higher predictions of the fatigue strength. Figure 13 presents these two groups for the investigated stress ratios of $R = -1$ and 0. It should be noted, that only these numerical results are depicted, where a run-out was achieved in the corresponding experiments.

Figure 13 shows a comparison between the numerically predicted fatigue strength and the stress range, which led to a run-out of the respective specimen. Herein, data points on the right-hand side of the diagonal line represent conservative estimations. Additionally, a scatter band of $+10\%$ and -10% was evaluated. As the majority of derived data points fall within the respective scatter band, the depicted results confirm the sound

applicability of the presented methodology to assess the fatigue strength of defect-afflicted cast steel components.

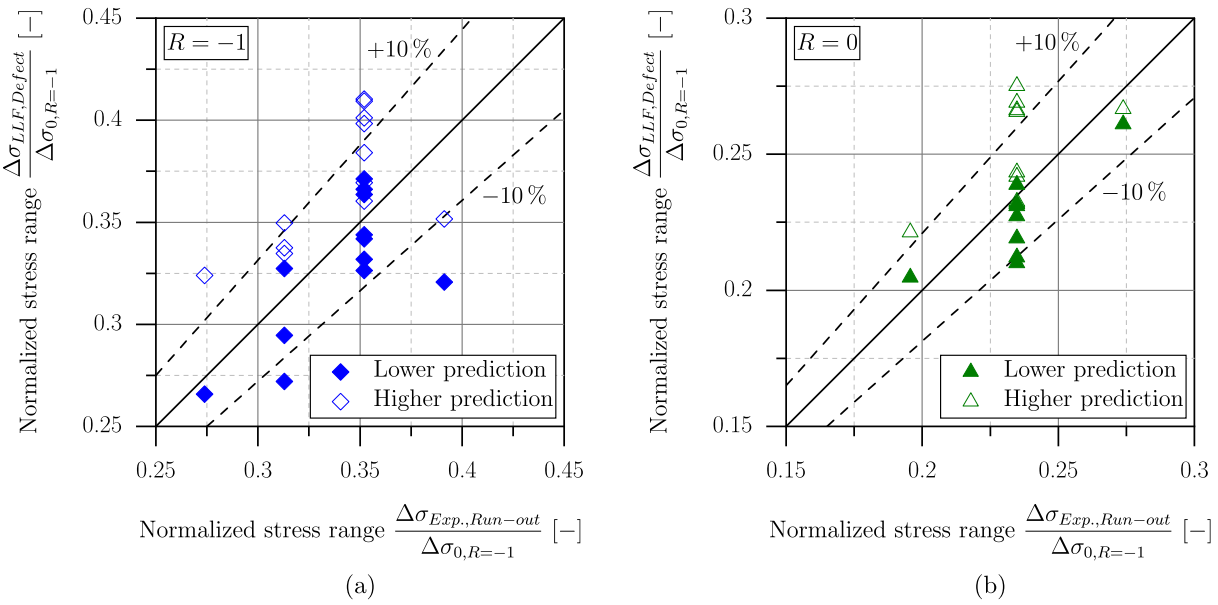

Figure 13. Comparison of the numerically and experimentally derived endurance limit results: (**a**) $R = -1$; and (**b**) $R = 0$.

Furthermore, the methodology presented in a preceding study [26] was applied, to assess the fatigue strength of the investigated defect-afflicted specimens based on the theory of critical distances. Utilizing the values of a_0 reported in Table 4, the fatigue strength $\Delta\sigma_{LLF,Defect,TCD}$ was evaluated by the TCD-framework. A comparison between the SED- and TCD-based assessment results is depicted in Figure 14. In contrast to Figure 13, the results of specimens where no run-out was achieved in the experiments are also depicted.

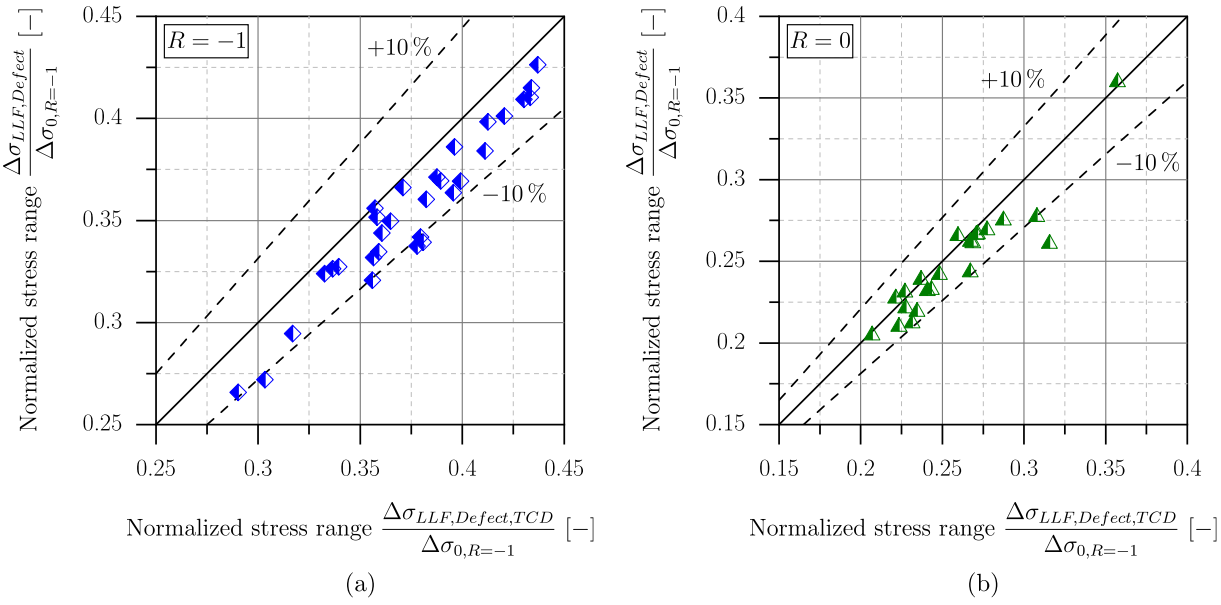

Figure 14. Comparison of SED- and TCD-based long-life fatigue assessment results: (**a**) $R = -1$; and (**b**) $R = 0$.

Regarding Figure 14, the SED-framework yields slightly reduced values of the predicted fatigue strength compared to the ones derived by the TCD-based methodology, indicating a higher degree of conservatism when utilizing the SED-framework. In order to

quantify the pictured tendencies, the average unsigned deviation $\Delta_{unsigned}$ and signed deviation Δ_{signed} between the numerically and experimentally derived results were evaluated according to Equation (8) and (9), respectively.

$$\Delta_{unsigned} = \frac{1}{n} \cdot \sum_{i=1}^{n} \frac{\left| \Delta\sigma_{LLF,Defect,i} - \Delta\sigma_{Exp.,Run-out,i} \right|}{\Delta\sigma_{Exp.,Run-out,i}} \cdot 100\% \tag{8}$$

$$\Delta_{signed} = \frac{1}{n} \cdot \sum_{i=1}^{n} \frac{\Delta\sigma_{LLF,Defect,i} - \Delta\sigma_{Exp.,Run-out,i}}{\Delta\sigma_{Exp.,Run-out,i}} \cdot 100\% \tag{9}$$

Table 7 summarizes the resulting deviations obtained by the SED- and TCD-based fatigue assessment methodologies.

Table 7. Average deviations obtained by the applied assessment methodologies.

R [−]	$\Delta_{unsigned}$ [%]		Δ_{signed} [%]	
	SED	**TCD**	**SED**	**TCD**
−1	8.6	11.3	+2.9	+9.2
0	7.0	7.4	+2.4	+5.4

Regarding Table 7, both applied methodologies led to similar values of $\Delta_{unsigned}$. As the maximum unsigned deviation takes a value of only 11.3%, the reported results emphasize the sound capability of the applied assessment concepts in predicting reasonable fatigue strength values of defect-afflicted cast steel components. Regarding the depicted values of Δ_{signed}, both concepts lead to positive deviations, which represent an average overestimation of experimentally derived run-out load levels. However, an improved prediction accuracy of the presented SED-based assessment methodology was observed, as the depicted values of Δ_{signed} are significantly smaller than those derived by the TCD-framework. This improved accuracy may be the result of the averaging procedure over a finite volume when applying the SED concept. Rather than assessing the fatigue life based on a single stress value at a dedicated point, as conducted in terms of the TCD, the SED-framework also considers the strains present in the control volume, yielding an improved contribution regarding size-effect. This increase in accuracy also justifies the slightly enhanced numerical effort of the sub-model-based SED-framework compared to the utilization of the TCD.

Concerning fatigue assessment in the finite-life region, the application of the SED depicts a more straight-forward approach compared to the TCD. Susmel and Taylor presented an extension of the TCD to facilitate the fatigue assessment of notched components in the medium-cycle regime, introducing a relationship between the critical distance and the number of cycles to failure [63]. This dependency is described by a power law, where the corresponding parameters are dependent on the material and the investigated load ratio. Hence, application of this methodology requires a calibration procedure in order to evaluate the corresponding material parameters. The subsequent fatigue assessment of defect-afflicted components is based on an iterative loop which increases numerical effort when dealing with arbitrarily shaped spatial imperfections. Considering the SED concept, the fatigue assessment in the finite-life regime takes advantage of the design limit curve evaluated in Section 3.1. Utilizing the derived parameter $\Delta\overline{W}^{(e)}_{97.5\%}$, the corresponding defect structure loaded under an arbitrary stress range $\Delta\sigma_i$ can be assessed following Equation (10).

$$\Delta\overline{W}^{(e)}_{DEF,97.5\%} = c_w \cdot \Delta\overline{W}^{(e)}_{97.5\%} \cdot \left(\frac{\Delta\sigma_i}{\Delta\sigma_g} \right)^2 \tag{10}$$

In order to also validate the presented methodology in the finite-life region, the stress ranges of all conducted experiments reported in Section 2.2 were considered according to

Equation (10), yielding corresponding values for the linear-elastic SED range $\Delta\overline{W}^{(e)}_{DEF,97.5\%}$. Figure 15 depicts the numerical assessment results of the defect-afflicted cast steel specimens, where the data points from Figure 8 are plotted as a reference.

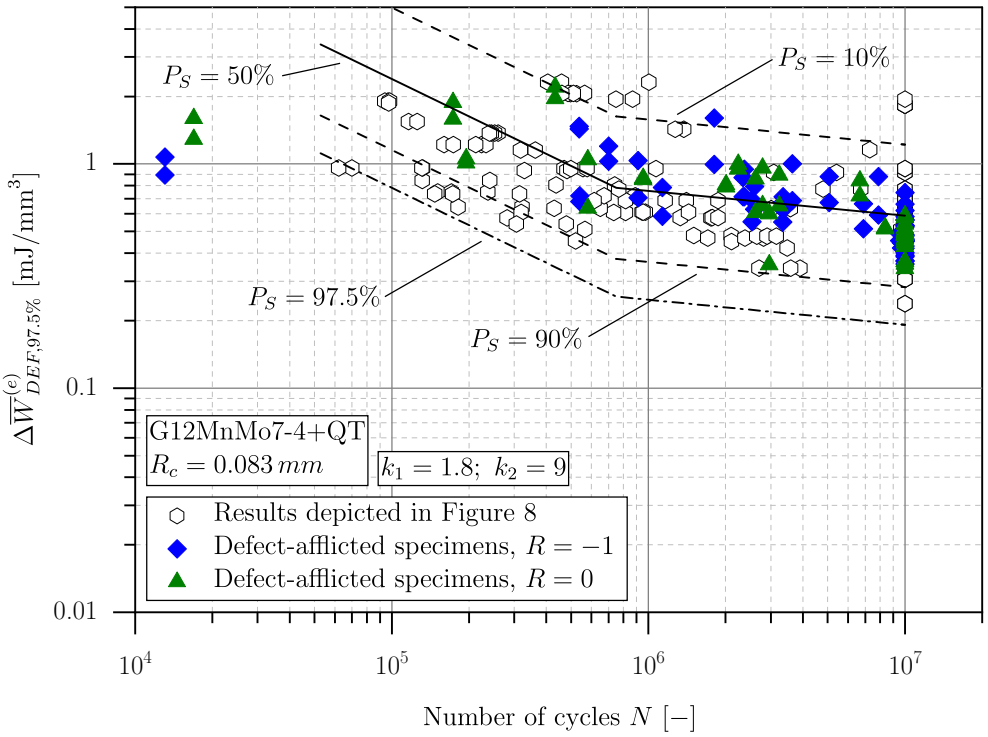

Figure 15. Fatigue assessment results of the defect-afflicted cast steel specimens.

Regarding the results of the defect-afflicted specimens, it should be mentioned, that there are two data points reported for each value of N, constituting the results based on the X- and Y-view of the corresponding specimen, respectively. As nearly all evaluated SED values fall within the derived scatter band, the depicted data points in Figure 15 exhibit satisfying fatigue assessment results. Looking closely in the region of $N = 10^4$, four data points can be observed, that are clearly outside the depicted scatter band. These data points represent the assessment results of specimens #04 tested at $R = -1$ and #26 tested at $R = 0$, while the fatigue strength of both specimens was accurately predicted by the presented methodology, the assessment of the respective stress ranges $\Delta\sigma_{Exp.,Failure}$ underestimates the SED value suggested by the evaluated scatter band. A possible explanation for the observed deviation could be a geometrical feature, representing a notch-like shape of high acuity, not visible on the two perpendicularly assessed radiographs. The utilization of three-dimensional finite element analyses could possibly improve the prediction accuracy, while simultaneously increasing the computational effort and associated costs. However, keeping in mind that the derived results solely rely upon linear-elastic simulations based on two planar projections of complex-shaped spatial imperfections per evaluated large–scale specimen, the presented methodology constitutes a well-applicable engineering-feasible tool for the fatigue assessment of defect-afflicted cast steel components.

4. Conclusions

Based on the results of the experimental and numerical work conducted in the present paper, the following scientific conclusions can be drawn:

- Based on the linear-elastic strain energy density concept, a design limit curve was evaluated for the high-strength cast steel alloy G12MnMo7-4+QT, summarizing the experimental results of three different specimen geometries tested at stress ratios of $R = -1$, 0 and 0.5 into a unique scatter band, characterized by a scatter index

of $1 : T_\sigma = 2.08$. The fatigue assessment results of notched specimens tested at $R = 0.5$ were overestimated by the linear-elastic framework. This overestimation was attributed to the occurring mean stress relaxation at high maximum stresses, leading to an effective stress ratio of $R < 0.5$.

- A numerical, energy-based methodology was presented to derive the parameter $\Delta\overline{W}^{(e)}_{97.5\%}$, characterizing the fatigue behaviour of cast steel components affected by inherent shrinkage porosities. Utilizing finite element simulations based on planar projections of corresponding spatial imperfections, $\Delta\overline{W}^{(e)}_{97.5\%}$ was statistically evaluated as the linear-elastic SED value, exceeding 97.5% of all SED values along the investigated defect contour. Utilization of $\Delta\overline{W}^{(e)}_{97.5\%}$ to assess the long-life fatigue strength of defect-afflicted cast steel specimens tested at stress ratios of $R = -1$ and 0 led to a sound agreement of the numerically and experimentally derived results.
- The application of a TCD-based long-life fatigue assessment methodology presented in a preceding study yielded fatigue strength values, which showed an overall match to the results obtained by the SED-framework. The energy-based assessment results revealed an improved prediction accuracy, contributing to the simultaneous consideration of stresses and strains in a finite region of highly-stressed material.
- Due to the linear-elastic framework, the derived fatigue parameter $\Delta\overline{W}^{(e)}_{97.5\%}$ can be utilized to assess components in the finite-life regime as well. The assessment of 33 defect-afflicted large–scale specimens led to reasonable fatigue-life predictions, merging into the scatter band of the derived fatigue curve. As the established linear-elastic simulation using sub-modelling provided a methodology based solely on planar projections of complex-shaped spatial defect structures, computational efforts were reduced, depicting the presented framework as an engineering-feasible tool to assess the fatigue behaviour of cast steel components affected by manufacturing process-based imperfections.

Further work might focus on the implementation of the non-linear material behaviour in terms of an elastic-plastic strain energy density approach. Ongoing work indicates that the application of the total strain energy density further narrows the scatter of the assessed data points, especially for high stress ratios. As the present study focusses on the assessment of defect-afflicted components subjected to uniaxial loading conditions, the investigation of multiaxial loading provides an interesting topic which should be addressed in future research work.

Author Contributions: Conceptualization, M.H., M.O. and M.S.; methodology, M.H.; software, M.H. and M.O.; validation, M.H., M.O. and M.S.; formal analysis, M.H. and M.O.; investigation, M.H. and M.O.; resources, M.S.; data curation, M.H.; writing—original draft preparation, M.H.; writing—review and editing, M.H., M.O. and M.S.; visualization, M.H.; supervision, M.S.; project administration, M.S.; funding acquisition, M.S. All authors have read and agreed to the published version of the manuscript.

Funding: This research was funded by the Austrian Federal Ministry for Digital and Economic Affairs and the National Foundation for Research, Technology, and Development.

Institutional Review Board Statement: Not applicable.

Data Availability Statement: Not applicable.

Acknowledgments: The financial support by the Austrian Federal Ministry for Digital and Economic Affairs and the National Foundation for Research, Technology and Development is gratefully acknowledged.

Conflicts of Interest: The authors declare no conflict of interest. The funders had no role in the design of the study, in the collection, analyses, or interpretation of data, in the writing of the manuscript, or in the decision to publish the results

Abbreviations

The following abbreviations are used in this manuscript:

$1:T_{\sigma}$	Scatter index in terms of stress
$1:T_{\Delta\overline{W}^{(e)}}$	Scatter index in terms of strain energy density
2α	Notch opening angle
λ_1	Williams' eigenvalue for mode I loading
ν	Poisson's ratio
ρ	Notch root radius
σ_{max}	Maximum stress
σ_{min}	Minimum stress
σ_{tip}	Stress at the notch tip
σ_{UTS}	Ultimate tensile strength
σ_{YS}	Yield strength
Δ_{signed}	Signed deviation
$\Delta_{unsigned}$	Unsigned deviation
$\Delta\varepsilon$	Strain range
$\Delta\sigma$	Stress range
$\Delta\sigma_0$	Plain material fatigue strength
$\Delta\sigma_{0,R=-1}$	Fatigue strength of the plain material tested at $R=-1$
$\Delta\sigma_g$	Stress range in the gross-section of the simulation models
$\Delta\sigma_i$	Stress range to be assessed
$\Delta\sigma_{Exp.,Failure}$	Stress range, where burst failure occurred in the experiment
$\Delta\sigma_{Exp.,Run\text{-}out}$	Stress range, where a run-out occurred in the experiment
$\Delta\sigma_{Exp.,Run-out,i}$	Stress range, where a run-out occurred in the i-th experiment
$\Delta\sigma_{LLF,Defect}$	Fatigue strength of the defect-afflicted component evaluated by SED concept
$\Delta\sigma_{LLF,Defect,i}$	Numerically evaluated fatigue strength of the i-th defect-afflicted component
$\Delta\sigma_{LLF,Defect,TCD}$	Fatigue strength of the imperfective component evaluated by TCD
ΔK	Stress intensity factor range
$\Delta K_{th,lc}$	Long-crack growth threshold stress intensity factor range
$\Delta K^{V}_{I,th}$	Long-crack growth threshold stress intensity factor range of a V-notched component
$\Delta W^{(e)}$	Linear-elastic strain energy density range
$\Delta\overline{W}^{(e)}$	Average linear-elastic strain energy density range
$\Delta\overline{W}^{(e)}_{97.5\%}$	Representative fatigue parameter
$\Delta\overline{W}^{(e)}_{DEF,97.5\%}$	Average elastic strain energy density range for an exceedance limit of 97.5%
$\Delta\overline{W}^{(e)}_{i}$	Linear-elastic strain energy density range averaged over Ω_i
Ω	Control volume
Ω_i	Control volume at node P_i
a_0	Material intrinsic length
c_w	Mean stress correction coefficient
da/dN	Crack propagation rate
e_1	Geometry parameter
n	Number of results
r_0	Distance between V-notch apex and origin of coordinate system
E	Young's modulus
$F(2\alpha)$	Geometry parameter dependent on 2α
$H(2\alpha, R_c/\rho)$	Geometry parameter dependent on 2α and R_c/ρ
N	Number of cycles
P_i	Node on the defect contour in the finite element model
P_S	Probability of survival
R	Stress ratio
R_c	Control radius
$\overline{W}^{(e)}$	Average linear-elastic strain energy density
FKM	Forschungskuratorium Maschinenbau
SED	Strain energy density
SENB	Single-edge-notched bending
TCD	Theory of critical distances

References

1. Santos, J.; Gouveia, R.M.; Silva, F. Designing a new sustainable approach to the change for lightweight materials in structural components used in truck industry. *J. Clean. Prod.* **2017**, *164*, 115–123. https://doi.org/10.1016/j.jclepro.2017.06.174.
2. Jung, S.; Jo, Y.H.; Jeon, C.; Choi, W.M.; Lee, B.J.; Oh, Y.J.; Kim, G.Y.; Jang, S.; Lee, S. Effects of Mn and Mo addition on high-temperature tensile properties in high-Ni-containing austenitic cast steels used for turbo-charger application. *Mater. Sci. Eng. A* **2017**, *682*, 147–155. https://doi.org/10.1016/j.msea.2016.11.006.
3. Bartlett, L.N.; Avila, B.R. Grain Refinement in Lightweight Advanced High-Strength Steel Castings. *Int. J. Met.* **2016**, *10*, 401–420. https://doi.org/10.1007/s40962-016-0048-0.
4. Druschitz, A.P.; Fitzgerald, D.C. Lightweight Iron and Steel Castings for Automotive Applications. In Proceedings of the SAE 2000 World Congress, Detroit, Michigan, 6–9 March 2000; Society of Automotive Engineers, Ed.; SAE International Commonwealth Drive: Warrendale, PA, USA, 2000; SAE Technical Paper Series. https://doi.org/10.4271/2000-01-0679.
5. Campbell, J. *Complete Casting Handbook: Metal Casting Processes, Techniques and Design*; Elsevier Butterworth-Heinemann: Oxford, UK, 2011.
6. Hardin, R.A.; Beckermann, C. Effect of Porosity on the Stiffness of Cast Steel. *Metall. Mater. Trans. A* **2007**, *38*, 2992–3006. https://doi.org/10.1007/s11661-007-9390-4.
7. Hardin, R.A.; Beckermann, C. Prediction of the Fatigue Life of Cast Steel Containing Shrinkage Porosity. *Metall. Mater. Trans. A* **2009**, *40*, 581–597. https://doi.org/10.1007/s11661-008-9755-3.
8. Hardin, R.A.; Beckermann, C. Effect of Porosity on Deformation, Damage, and Fracture of Cast Steel. *Metall. Mater. Trans. A* **2013**, *44*, 5316–5332. https://doi.org/10.1007/s11661-013-1669-z.
9. Makino, T.; Shimokawa, Y.; Yamamoto, M. Fatigue Property and Design Criterion of Cast Steel for Railway Bogie Frames. *Mater. Trans.* **2019**, *60*, 950–958. https://doi.org/10.2320/matertrans.Z-M2019814.
10. Nagel, S.; Rauber, C.; Veile, I.; Knödel, P.; Ummenhofer, T. Influence of internal imperfections on the fatigue resistance of cast steel – testing methodology. *MATEC Web Conf.* **2019**, *300*, 09001. https://doi.org/10.1051/matecconf/201930009001.
11. Schuscha, M.; Horvath, M.; Leitner, M.; Stoschka, M. Notch Stress Intensity Factor (NSIF)-Based Fatigue Design to Assess Cast Steel Porosity and Related Artificially Generated Imperfections. *Metals* **2019**, *9*, 1097. https://doi.org/10.3390/met9101097.
12. Rennert, R.; Kullig, E.; Vormwald, M. *Analytical Strength Assessment of Components Made of Steel, Cast Iron and Aluminium Materials in Mechanical Engineering: FKM Guideline*, 6th ed.; VDMA Verl.: Frankfurt am Main, Germany, 2012.
13. Taylor, D. Geometrical effects in fatigue: A unifying theoretical model. *Int. J. Fatigue* **1999**, *21*, 413–420. https://doi.org/10.1016/S0142-1123(99)00007-9.
14. El Haddad, M.H.; Topper, T.H.; Smith, K.N. Prediction of non propagating cracks. *Eng. Fract. Mech.* **1979**, *11*, 573–584. https://doi.org/10.1016/0013-7944(79)90081-X.
15. Cicero, S.; Madrazo, V.; Carrascal, I.A. Analysis of notch effect in PMMA using the Theory of Critical Distances. *Eng. Fract. Mech.* **2012**, *86*, 56–72. https://doi.org/10.1016/j.engfracmech.2012.02.015.
16. Susmel, L.; Taylor, D. The theory of critical distances to predict static strength of notched brittle components subjected to mixed-mode loading. *Eng. Fract. Mech.* **2008**, *75*, 534–550. https://doi.org/10.1016/j.engfracmech.2007.03.035.
17. Chiandussi, G.; Rossetto, M. Evaluation of the fatigue strength of notched specimens by the point and line methods with high stress ratios. *Cumul. Fatigue Damage Conf. -Univ. Seville 2003 Cumul. Fatigue Damage Conf.* **2005**, *27*, 639–650. https://doi.org/10.1016/j.ijfatigue.2004.11.006.
18. Susmel, L.; Taylor, D. The Theory of Critical Distances to estimate lifetime of notched components subjected to variable amplitude uniaxial fatigue loading. *Cumul. Fatigue Damage Conf.* **2011**, *33*, 900–911. https://doi.org/10.1016/j.ijfatigue.2011.01.012.
19. Susmel, L. The theory of critical distances: A review of its applications in fatigue. *Eng. Fract. Mech.* **2008**, *75*, 1706–1724. https://doi.org/10.1016/j.engfracmech.2006.12.004.
20. Taylor, D. Analysis of fatigue failures in components using the theory of critical distances. *Eng. Fail. Anal.* **2005**, *12*, 906–914. https://doi.org/10.1016/j.engfailanal.2004.12.007.
21. González, P.; Cicero, S.; Arroyo, B.; Álvarez, J.A. A Theory of Critical Distances based methodology for the analysis of environmentally assisted cracking in steels. *Eng. Fract. Mech.* **2019**, *214*, 134–148. https://doi.org/10.1016/j.engfracmech.2019.04.004.
22. Negru, R.; Marsavina, L.; Voiconi, T.; Linul, E.; Filipescu, H.; Belgiu, G. Application of TCD for brittle fracture of notched PUR materials. *Theor. Appl. Fract. Mech.* **2015**, *80*, 87–95. https://doi.org/10.1016/j.tafmec.2015.05.005.
23. He, J.C.; Zhu, S.P.; Liao, D.; Niu, X.P.; Gao, J.W.; Huang, H.Z. Combined TCD and HSV approach for probabilistic assessment of notch fatigue considering size effect. *Eng. Fail. Anal.* **2021**, *120*, 105093. https://doi.org/10.1016/j.engfailanal.2020.105093.
24. Stoschka, M.; Horvath, M.; Fladischer, S.; Oberreiter, M. Study of Local Fatigue Methods (TCD, N-SIF, and ESED) on Notches and Defects Related to Numerical Efficiency. *Appl. Sci.* **2023**, *13*, 2247. https://doi.org/10.3390/app13042247.
25. Chen, C.; Jie, Z.; Wang, K. Fatigue life evaluation of high-strength steel wires with multiple corrosion pits based on the TCD. *J. Constr. Steel Res.* **2021**, *186*, 106913. https://doi.org/10.1016/j.jcsr.2021.106913.
26. Horvath, M.; Stoschka, M.; Fladischer, S. Fatigue strength study based on geometric shape of bulk defects in cast steel. *Int. J. Fatigue* **2022**, *163*, 107082. https://doi.org/10.1016/j.ijfatigue.2022.107082.
27. Lazzarin, P.; Berto, F. Some Expressions for the Strain Energy in a Finite Volume Surrounding the Root of Blunt V-notches. *Int. J. Fract.* **2005**, *135*, 161–185. https://doi.org/10.1007/s10704-005-3943-6.

28. Lazzarin, P.; Zambardi, R. A finite-volume-energy based approach to predict the static and fatigue behavior of components with sharp V-shaped notches. *Int. J. Fract.* **2001**, *112*, 275–298. https://doi.org/10.1023/A:1013595930617.
29. Atzori, B.; Lazzarin, P.; Meneghetti, G. A unified treatment of the mode I fatigue limit of components containing notches or defects. *Int. J. Fract.* **2005**, *133*, 61–87. https://doi.org/10.1007/s10704-005-2183-0.
30. Williams, M.L. Stress Singularities Resulting From Various Boundary Conditions in Angular Corners of Plates in Extension. *J. Appl. Mech.* **1952**, *19*, 526–528.
31. Yosibash, Z.; Bussiba, A.; Gilad, I. Failure criteria for brittle elastic materials. *Int. J. Fract.* **2004**, *125*, 307–333. https://doi.org/10.1023/B:FRAC.0000022244.31825.3b.
32. Berto, F.; Lazzarin, P. A review of the volume-based strain energy density approach applied to V-notches and welded structures. *Theor. Appl. Fract. Mech.* **2009**, *52*, 183–194. https://doi.org/10.1016/j.tafmec.2009.10.001.
33. Schuscha, M.; Leitner, M.; Stoschka, M.; Meneghetti, G. Local strain energy density approach to assess the fatigue strength of sharp and blunt V-notches in cast steel. *Int. J. Fatigue* **2020**, *132*, 105334. https://doi.org/10.1016/j.ijfatigue.2019.105334.
34. Ellyin, F.; Kujawski, D. Plastic Strain Energy in Fatigue Failure. *J. Press. Vessel Technol.* **1984**, *106*, 342–347. https://doi.org/10.1115/1.3264362.
35. Lazzarin, P.; Sonsino, C.M.; Zambardi, R. A notch stress intensity approach to assess the multiaxial fatigue strength of welded tube-to-flange joints subjected to combined loadings. *Fatigue Fract. Eng. Mater. Struct.* **2004**, *27*, 127–140. https://doi.org/10.1111/j.1460-2695.2004.00733.x.
36. Livieri, P.; Lazzarin, P. Fatigue strength of steel and aluminium welded joints based on generalised stress intensity factors and local strain energy values. *Int. J. Fract.* **2005**, *133*, 247–276. https://doi.org/10.1007/s10704-005-4043-3.
37. Gómez, F.J.; Elices, M.; Berto, F.; Lazzarin, P. Local strain energy to assess the static failure of U-notches in plates under mixed mode loading. *Int. J. Fract.* **2007**, *145*, 29–45. https://doi.org/10.1007/s10704-007-9104-3.
38. Lazzarin, P.; Livieri, P.; Berto, F.; Zappalorto, M. Local strain energy density and fatigue strength of welded joints under uniaxial and multiaxial loading. *Eng. Fract. Mech.* **2008**, *75*, 1875–1889. https://doi.org/10.1016/j.engfracmech.2006.10.019.
39. Lazzarin, P.; Berto, F.; Elices, M.; Gómez, J. Brittle failures from U- and V-notches in mode I and mixed, I + II, mode: A synthesis based on the strain energy density averaged on finite-size volumes. *Fatigue Fract. Eng. Mater. Struct.* **2009**, *32*, 671–684. https://doi.org/10.1111/j.1460-2695.2009.01373.x.
40. Gallo, P.; Berto, F. Advanced Materials for Applications at High Temperature: Fatigue Assessment by Means of Local Strain Energy Density. *Adv. Eng. Mater.* **2016**, *18*, 2010–2017. https://doi.org/10.1002/adem.201500547.
41. Razavi, S.; Ferro, P.; Berto, F.; Torgersen, J. Fatigue strength of blunt V-notched specimens produced by selective laser melting of Ti-6Al-4V. *Theor. Appl. Fract. Mech.* **2017**, *97*, 376–384. https://doi.org/10.1016/j.tafmec.2017.06.021.
42. Foti, P.; Berto, F. Fatigue assessment of high strength welded joints through the strain energy density method. *Fatigue Fract. Eng. Mater. Struct.* **2020**, *43*, 2694–2702. https://doi.org/10.1111/ffe.13336.
43. Foti, P.; Santonocito, D.; Risitano, G.; Berto, F. Fatigue assessment of cruciform joints: Comparison between Strain Energy Density predictions and current standards and recommendations. *Eng. Struct.* **2021**, *230*, 111708. https://doi.org/10.1016/j.engstruct.2020.111708.
44. Ding, K.; Yang, Y.; Wang, Z.; Zhang, T.; Guo, W. Relationship between local strain energy density and fatigue life of riveted Al-Li alloy plate. *Theor. Appl. Fract. Mech.* **2022**, 103672. https://doi.org/10.1016/j.tafmec.2022.103672.
45. *SEW 520*; Hochfester Stahlguß mit guter Schweißeignung; Technical Rule. Verlag Stahleisen GmbH: Düsseldorf, Germany, 1996.
46. Schuscha, M.; Leitner, M.; Stoschka, M.; Pusterhofer, S.; Meneghetti, G. Numerical crack growth study on porosity afflicted cast steel specimens. *Frat. Ed Integrità Strutt.* **2019**, *13*, 58–69. https://doi.org/10.3221/IGF-ESIS.48.08.
47. *ASTM E446*; Standard Reference Radiographs for Steel Castings Up to 2 in. (50.8 mm) in Thickness. ASTM International: West Conshohocken, PA, USA, 2020. https://doi.org/10.1520/E0446-20.
48. Tabernig, B.; Pippan, R. Determination of the length dependence of the threshold for fatigue crack propagation. *Eng. Fract. Mech.* **2002**, *69*, 899–907. https://doi.org/10.1016/S0013-7944(01)00129-1.
49. Newman, J.C., Jr.; Yamada, Y. Compression precracking methods to generate near-threshold fatigue-crack-growth-rate data. *Int. J. Fatigue* **2010**, *32*, 879–885. https://doi.org/10.1016/j.ijfatigue.2009.02.030.
50. Newman Jr., J.; Schneider, J.; Daniel, A.; McKnight, D. Compression pre-cracking to generate near threshold fatigue-crack-growth rates in two aluminum alloys. *Int. J. Fatigue* **2005**, *27*, 1432–1440. https://doi.org/10.1016/j.ijfatigue.2005.07.006.
51. Oberreiter, M.; Aigner, R.; Pomberger, S.; Leitner, M.; Stoschka, M. Impact of microstructural properties on the crack threshold of aluminium castings. *Eng. Fract. Mech.* **2021**, *241*, 107431. https://doi.org/10.1016/j.engfracmech.2020.107431.
52. Elber, W. Fatigue crack closure under cyclic tension. *Eng. Fract. Mech.* **1970**, *2*, 37–45. https://doi.org/10.1016/0013-7944(70)90028-7.
53. Newman, J.C. A crack opening stress equation for fatigue crack growth. *Int. J. Fract.* **1984**, *24*, R131–R135. https://doi.org/10.1007/BF00020751.
54. Mettu, S.; Shivakumar, V.; Beek, J.; Yeh, F.; Williams, L.; Forman, R.; McMahon, J.; Newman, I. NASGRO 3.0: A software for analyzing aging aircraft. In Proceedings of the Second Joint NASA/FAA/DoD Conference on Aging Aircraft, Williamsburg, Virginia, 31 August–3 September 1998; NASA Langley Research Center, Ed.; 1999; pp. 792–801.
55. Maierhofer, J.; Pippan, R.; Gänser, H.P. Modified NASGRO equation for physically short cracks. *Int. J. Fatigue* **2014**, *59*, 200–207. https://doi.org/10.1016/j.ijfatigue.2013.08.019.

56. Tanaka, K.; Nakai, Y.; Yamashita, M. Fatigue growth threshold of small cracks. *Int. J. Fract.* **1981**, *17*, 519–533. https://doi.org/10.1007/BF00033345.
57. *ASTM E739*; Standard Practice for Statistical Analysis of Linear or Linearized Stress-Life (S-N) and Strain-Life (e-N) Fatigue Data. ASTM International: West Conshohocken, PA, USA, 1991.https://doi.org/10.1520/E0739-91R98.
58. Dengel, D. Die arc sin $\sqrt{}$P-Transformation—Ein einfaches Verfahren zur grafischen und rechnerischen Auswertung geplanter Wöhlerversuche. *Mater. Und Werkst.* **1975**, *6*, 253–261. https://doi.org/10.1002/mawe.19750060803.
59. Morrow, J.; Sinclair, G.M. Cycle-Dependent Stress Relaxation. In Proceedings of the Symposium on Basic Mechanisms of Fatigue, Boston, MA, USA, 23 June 1958; American Society for Testing and Materials, Ed.; ASTM International: West Conshohocken, PA, USA, 1959; pp. 83–99. https://doi.org/10.1520/STP39312S.
60. Landgraf, R.W.; Chernenkoff, R.A. Residual stress effects on fatigue of surface processed steels. *Anal. Exp. Methods Residual Stress Eff. Fatigue, ASTM STP* **1988**, *1004*, 1–12.
61. Vollmer, J.; Mencl, R.; Muller, H. Improved Laplacian Smoothing of Noisy Surface Meshes. *Comput. Graph. Forum* **1999**, *18*, 131–138. https://doi.org/10.1111/1467-8659.00334.
62. Lazzarin, P.; Berto, F. Control volumes and strain energy density under small and large scale yielding due to tension and torsion loading. *Fatigue Fract. Eng. Mater. Struct.* **2008**, *31*, 95–107. https://doi.org/10.1111/j.1460-2695.2007.01206.x.
63. Susmel, L.; Taylor, D. A novel formulation of the theory of critical distances to estimate lifetime of notched components in the medium-cycle fatigue regime. *Fatigue Fract. Eng. Mater. Struct.* **2007**, *30*, 567–581. https://doi.org/10.1111/j.1460-2695.2007.01122.x.